ACS Photonics

Article

Cite This: ACS Photonics 2018, 5, 4484−4490

pubs.acs.org/journal/apchd5

Epsilon-Near-Zero Si Slot-Waveguide Modulator

Xiaoge Liu,[†] Kai Zang,[‡] Ju-Hyung Kang,[†] Junghyun Park,[†] James S. Harris,[‡] Pieter G. Kik,[†,§] and Mark L. Brongersma*[,†]

[†]Geballe Laboratory for Advanced Materials and [‡]Department of Electrical Engineering, Stanford University, Stanford, California 94305, United States

[§]CREOL, The College of Optics and Photonics, University of Central Florida, 4000 Central Florida Blvd, Orlando, Florida 32816, United States

Supporting Information

ABSTRACT: We experimentally demonstrate a broadband electro-absorption modulator exploiting indium tin oxide (ITO) as the active switching material. Si strip waveguides are fabricated and covered with 8 nm of HfO_2 and 15 nm of ITO to form metal-oxide-semiconductor capacitor (MOS-C) based modulators. The mobile carrier density in the ITO film is controlled using a postanneal treatment to tune its permittivity ε to a near-zero value at the operation wavelength of 1550 nm. Using simulations and experiments, we demonstrate that realizing an epsilon-near-zero (ENZ) can enhance the modulation performance as it increases the overlap of the guided mode with the active ITO layer. We then show even greater benefits of this approach with Si waveguides featuring a central slot filled with ITO. Leveraging the ENZ effect, we achieve a notable 3 dB modulation depth of optical signals in a nonresonant waveguide structure with a length of 20 μm. The results provide insight into the design of very compact modulators for chip-scale optical links.

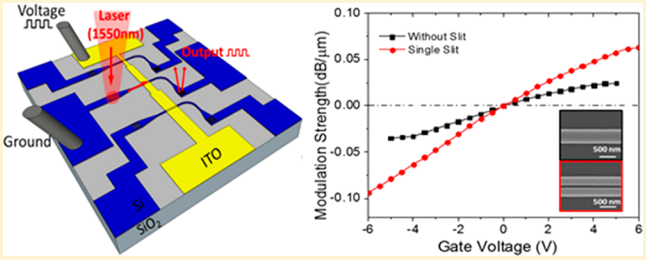

KEYWORDS: *silicon photonics, electro-absorption modulator, transparent conducting oxide, epsilon-near-zero material*

With the ever-increasing demand for computing power, the performance bottleneck has shifted from individual transistors to the interconnection network between transistors.[1] On-chip optical links can provide a key breakthrough in reducing power consumption in chips.[1−3] However, new concepts for realizing high-speed, ultracompact, and power-efficient electro-optic modulators are needed to realize this vision.[4,5] This is because current modulator designs that exploit weak electro-optical effect in silicon (Si) tend to require a large device footprint that comes with an undesirably large capacitance.[6] Si modulators integrated with high-Q optical resonators can increase the modulation strength for a given footprint, but suffer from a reduced bandwidth and thermal instabilities.[7] Modulators that leverage the beneficial optical properties of germanium and compound semiconductors face notable integration challenges with existing Si platforms.[8−10] Plasmonic modulators offer high field confinement capable of boosting electro-optic effects, but the high intrinsic loss that comes with using metals hinders their application.[11] Graphene-based modulators have achieved high modulation efficiencies by electrically tuning the Fermi level of graphene, but it is challenging to realize a good modal overlap with an atomically thin material.[12,13]

Strong electro-optic effects have recently been observed in transparent conductive oxides. The Si-compatible material, indium tin oxide (ITO), has proven to be a particularly promising candidate for integration into modulators.[4,14] The optical properties of ITO can be electrically tuned by changing its electron density.[4,15,16] Both accumulation and depletion of mobile electrons in ITO films has been achieved by applying an electrical gate bias, and this can change its permittivity in the near-infrared regime from a positive value (dielectric-like) to a negative value (metallic-like).[17,18] When the permittivity of the ITO material is tuned to be close to zero, which is referred to as the "epsilon-near-zero" (ENZ) state, the absorption losses inside the ITO material can effectively be changed and open the door to realizing very strong electro-optic effects.[19−22] For this reason, ENZ electro-absorption modulators show great potential for achieving a large modulation strength.[4,14] In this paper, we experimentally demonstrate a broadband, ultracompact, Si waveguide modulator exploiting the ENZ effect in ITO.

ITO behaves as a free electron Drude metal whose optical properties are governed by its mobile carrier density.[23,24] The optical permittivity of ITO can be described as

$$\varepsilon_{\mathrm{ITO}} = \varepsilon_{\infty} - \frac{\omega_p^2}{\omega^2 + i\omega\Gamma}, \quad \omega_p^2 = \frac{ne^2}{\varepsilon_0 m^*}$$

where ε_{∞} is the background dielectric constant, ω is the angular frequency of light, and Γ is the collision frequency for

Received: July 11, 2018
Published: October 4, 2018

DOI: 10.1021/acsphotonics.8b00945
ACS Photonics 2018, 5, 4484−4490

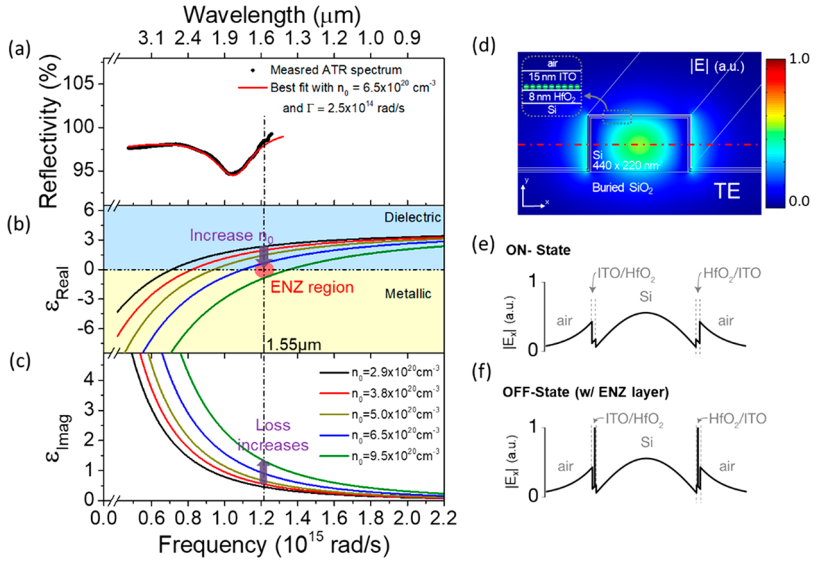

Figure 1. ITO characterization and modulator operation mechanism using the ENZ effect. (a) ATR spectrum of an ITO/Au/quartz film stack for ITO material characterization. The black curve shows experimental results and the blue curve shows a simulation that best fits the experimental data. (b) The real part of the Drude-model permittivity for ITO films with different carrier densities that can be realized by changing the postdeposition annealing treatment. The Drude parameters are extracted by fitting to the ATR experimental curves. The top blue area in the graph represents the dielectric-like region of ITO and the bottom yellow part represents the metallic-like region of ITO. The red circle highlights the ENZ region near the modulator's operation wavelength of 1.55 μm (vertical dashed line). (c) The imaginary part of the Drude-model permittivity of ITO films with different carrier densities. (d) Cross sectional view of the proposed waveguide modulator design. It shows a 440 × 220 nm^2 Si strip waveguide on top of a 3 μm thick SiO_2 base that is overcoated with 8 nm thick HfO_2 and 15 nm thick ITO layers. The color map shows the normalized electric field intensity profile of the fundamental TE mode of the Si waveguide. Electrons are accumulated at the ITO/HfO_2 interface in the OFF-state. (e) Electrical field profile of the guided mode plotted along the red dashed line shown in the waveguide cross section in panel (d) for the ON-state without gate bias. (f) Electrical field profile along the red dashed line in panel (d) for the OFF-state with an applied gate bias. In this state, the electrical field is strongly enhanced inside the ENZ region.

the mobile electrons in ITO. The plasma frequency of ITO ω_p depends on the carrier concentration n, electron charge e, vacuum permittivity ε_0, and effective mass of electrons in the ITO film m^* (see ref 23). The carrier density of ITO can be passively tuned by thermal annealing[23] or actively tuned by electrical gating[15,17] as well as optical excitation.[25,26]

The optical properties of ITO films can be characterized by attenuated total reflection (ATR) measurements in which surface plasmons are excited.[23,24,27] Figure 1a shows an example of an ATR measurement on an ITO/Au/quartz stack with a 15 nm thick ITO layer and a 50 nm thick Au film (black dots). The presence of the ITO layer produces a reflection dip in the ATR spectrum due to the resonance at the surface plasmon frequency ω_{SP} of ITO, where the ITO's permittivity is close to the negative value of air's permittivity ($\varepsilon_{ITO} = -\varepsilon_{air}$, $\omega_{SP} \approx \frac{\omega_p}{\sqrt{\epsilon_\infty + \epsilon_{air}}}$). The spectral location of the reflection dip is determined by ω_p and the width of the dip is governed by Γ. The ATR spectrum can be simulated using the transfer matrix method (TMM; blue curve in Figure 1a), and the Drude model parameters such as ω_p and Γ can be extracted from the best fit to the experimental data.[23] The blue curve in Figure 1a shows such a fit for an ITO film with a carrier concentration of $n = 6.5 \times 10^{20}$ cm^{-3} and $\Gamma = 2.5 \times 10^{14}$ rad/s.

To identify the optimum optical properties for modulation, several ITO films were grown and received different postannealing treatments to tune the intrinsic electron density of ITO from 2.9×10^{20} cm^{-3} to 9.5×10^{20} cm^{-3} (see Methods). The real and imaginary value of the permittivities are extracted for those films from best fits to the data (Figure 1b for the real part ε_{Real} and in Figure 1c for the imaginary part ε_{Imag}). The real part of ITO's permittivity is negative at low frequencies and monotonically grows with increasing frequency to ultimately become positive-valued. At a specific frequency ($\omega_{ENZ} \approx \frac{\omega_p}{\sqrt{\epsilon_\infty}}$), the magnitude of the permittivity is close to zero $|\varepsilon_{ENZ}| \approx 0$, known as the ENZ point. As the carrier concentration is increased, the permittivity curves shift and the ENZ point moves to a higher frequency. Knowledge of these permittivity curves facilitates the design of our modulator, in which we will aim to achieve similar changes in the optical properties by electrically induced charge accumulation and depletion. For the optimum performance, we will show in theory and experiment that it is beneficial to operate close to the ENZ point. In order to achieve that, we optimize our anneal treatment and thus initial carrier concentration.

Our ITO-based modulator design consists of a Si strip waveguide (440 × 220 nm^2) on top of a buried SiO_2 layer coated with an 8 nm thick hafnium oxide (HfO_2) layer and a 15 nm thick ITO layer (Figure 1d). This waveguide supports a transverse electric-like (TE) mode with the dominant electric field component along the horizontal direction (see Figure 1d).[14] The ITO/HfO_2/Si stack forms a metal-oxide-semiconductor capacitor (MOS-C) with the ITO effectively serving as the metallic gate electrode and the HfO_2 operating as the gate dielectric. The ITO film is chosen to have a relatively low carrier concentration ($n = 6.5 \times 10^{20}$ cm^{-3}) so that it behaves as a dielectric material with a positive permittivity of $\varepsilon_{Real} = 0.6$ at the operating wavelength of 1.55 μm (blue line in Figure 1b). In the ON-state with no applied bias, Figure 1e plots the horizontal mode-profile along the red dashed line shown in

DOI: 10.1021/acsphotonics.8b00945
ACS Photonics 2018, 5, 4484−4490

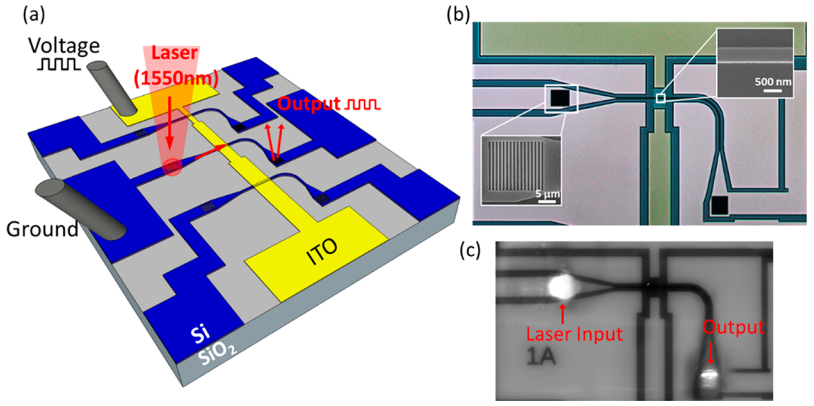

Figure 2. Schematic of the proposed modulator and fabrication results. (a) The design of an ITO-based ENZ modulator. Grating couplers couple free-space light into and out of a Si waveguide (blue). The waveguides features a 90° bend to allow for high signal-to-background cross-polarization measurements. The ITO material (yellow) and Si waveguides are connected to wire-bonded electrical pads. To quantify the modulation strength per unit length, we create a number of devices in which different lengths of the Si guides are covered with ITO material. (b) Top-view optical image of a fabricated modulator. The insets show SEM images with scale bars inside for a grating coupler and a waveguide. (c) Optical image of a laser modulation experiment in which 1550 nm laser light couples into the waveguide at the input grating coupler. The laser light is transmitted through the bent waveguide and then couples out at the output coupler.

Figure 1d. In this state, there is no strong field in the ITO layer and the ITO material resembles a low-loss dielectric. As a result, light propagating down the ITO-coated Si waveguide does not experience significant optical loss. In the OFF-state with a −5 V applied gate bias, electrons accumulate in the ITO material and the resulting high-carrier-density layer can turn into an ENZ region, as predicted by the Drude model (purple arrow and red circle in Figure 1b). The normal component of the electric displacement field ($D_n = \varepsilon E_n$) of the guided optical mode has to be continuous across the materials boundary. As a result, the electric field magnitude inside the ENZ material displays a notable enhancement with respect to the adjacent Si waveguide by the ratio of the permittivity magnitudes for Si and ITO.

For our fabricated ITO film, the electric field in the accumulation layer of ITO is eventually boosted by a factor of 3.6, given $n = 6.5 \times 10^{20}$ cm^{-3} and $\Gamma = 2.5 \times 10^{14}$ rad/s. Figure 1f plots the electrical field distribution profile under gate bias and shows a strong field boost inside the ITO layer. The ENZ accumulation layer effectively redistributes the optical mode to create a more favorable overlap with the active ITO switching layer. Meanwhile, the imaginary part of the permittivity ε_{Imag} in the accumulation layer also increases to further boost the materials absorption (purple arrow in Figure 1c). Since the increasing material loss and enhanced mode overlap occur simultaneously, the absorption P_{absorb} is maximized inside the ENZ layer where $P_{absorb} \propto \varepsilon_{Imag}E^2 \propto \varepsilon_{Imag}/|\varepsilon_{ENZ}|^2$. Thus, the transmitted signal is absorbed significantly more effectively by applying the electrical gating bias and a large modulation strength can be achieved.

Figure 2a schematically shows our modulator design and Figure 2b shows an optical image of a fabricated device. Scanning electron microscope (SEM) images of a grating coupler and the Si waveguide are also shown as insets. We use tapered grating couplers with a 1 μm period and 0.5 filling factor to couple a normally incident, free-space laser beam into and out of the waveguide (Figure 2c).[28,29] A bent waveguide design is used to facilitate a cross-polarization measurement of the light transmission through the waveguide in which any unwanted background light that is not transmitted through the Si guide is removed (e.g., scattered light from the grating coupler and reflected light from the substrate).[4] An 8 nm-thick HfO_2 film is deposited to create an insulating layer on top of the waveguide and then a 15 nm-thick layer of ITO is deposited by magnetron sputtering. ITO strips of different width are defined to create modulators with different interaction length (see Methods). This facilitates an experimental determination of the modulation strength per unit length. There are larger Si and ITO pads for electrical wire bonding to apply a gate bias. The gate bias is applied to the ITO/HfO_2/Si stack to electrically accumulate/deplete electrons inside the ITO layer. Figure 2c presents the optical image during an experiment in which the signal laser spot illuminates the input-coupler and an output signal reemerges from the output-coupler. An ultrafast photodiode is used to detect the transmitted light emerging from the output-coupler. More information on the setup can be found in the Methods and Supporting Information.

In the modulation experiments, the output signal is controlled with a gate bias applied between the ITO and Si, across the HfO_2 layer. Figure 3a shows the experimentally observed changes in the output light intensity versus the applied bias (black data points and curve). Here, the device has a 30-μm-long waveguide section covered with ITO and is annealed in forming gas at 230 °C for 10 min. According to the ATR characterization, this ITO film has a carrier concentration of 6.5×10^{20} cm^{-3} without an applied bias (blue curve in Figure 1b). Compared to the unbiased output signal, the transmitted signal intensity decreases when we apply a negative bias to accumulate carriers in the ITO layer and the intensity increases when we apply a positive bias to deplete the film. The normalized output intensity changes from 74% to 120% at 1550 nm. The modulation curve displays hysteresis at first, but this disappears after several modulation cycles (see Supporting Information).

The modulation results are analyzed in a quantitative manner (red curve in Figure 3a) with the help of finite-difference time-domain (FDTD) simulations. The inset to Figure 3a presents the simulated TE mode field distribution of the waveguide. The imaginary part of the effective mode index for this mode quantifies the optical propagation loss.[30] For the red square region shown in the inset to Figure 3a, we plot the

DOI: 10.1021/acsphotonics.8b00945
ACS Photonics 2018, 5, 4484−4490

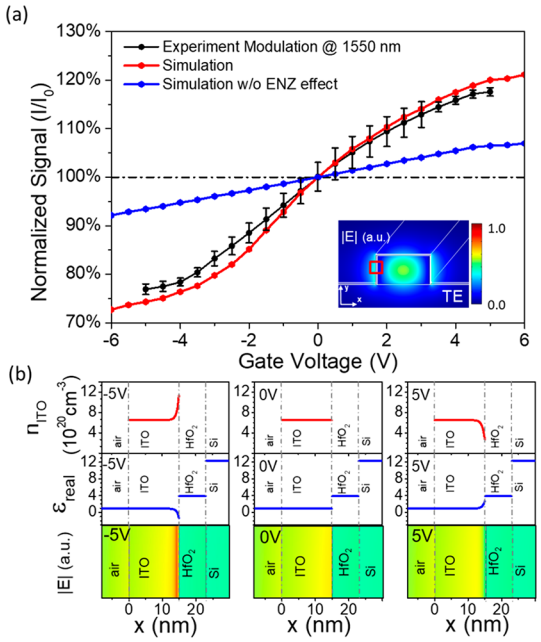

Figure 3. Signal modulation experiments and simulation results. (a) Output signal intensity versus applied gate bias for a 30-μm-long ENZ modulator. The left axis plots the output signal intensity normalized to the output signal without bias. The black curve represents the experimental results with error bars calculated from multiple measurements. The red curve represents the simulation results with the beneficial ENZ effect while the blue curve represents the simulation without the ENZ effect. The inset shows a mode profile analysis of the modulator at a 0 V applied bias. (b) Plots of the electron density, permittivity and electric field distribution change in the red square region shown in the inset to panel (a) and for applied gate bias values of −5 V (left panel), 0 V (middle panel) and 5 V (right panel). The top row shows the electron density of ITO n_{ITO} across the air/ITO/HfO_2/Si stack. The middle row shows the real part of the permittivity for air, ITO, HfO_2 and Si. The permittivity of the ITO changes with an applied gate bias while the other materials remain unchanged. The bottom row shows a zoom-in of the red square region depicted in the inset to (a) for various applied gate bias values and show the electrical field distribution in the stack.

electron density, material permittivity and electrical field distributions to see how they vary across the air/ITO/HfO_2/Si stack (see Figure 3b). The left panel of Figure 3b represents the case in which a −5 V gate bias is applied. It shows the accumulated electron density n_{ITO} inside the ITO layer near the ITO/HfO_2 interface as calculated from the Poisson equation and resulting from band bending.[15,31] Inside the accumulation layer, the real part of ITO's permittivity ε_{Real} decreases based on the Drude model, which is also shown in the panel. The permittivity of the other materials are unaffected by the applied bias. As the ITO accumulation layer turns into an ENZ material, the electrical field is strongly enhanced close to the ITO/HfO_2 interface (the bottom part of the left panel in Figure 3b). The creation of an ENZ layer induces a strong electro-absorption effect and the transmitted signal is suppressed (red curve in Figure 3a at −5 V). The middle panel of Figure 3b represents the case of 0 V gate bias. Here, the electrical field distribution inside ITO remains uniform. The right panel of Figure 3b represents the case in which a positive 5 V gate bias is applied. This results in a depletion of the ITO layer near the ITO/HfO_2 interface and the real permittivity of ITO ε_{real} curves upward. This results in a decreased electrical field inside the depletion region (the right panel of Figure 3b). Since the optical mode is redistributed so that it is effectively pushed out of the absorptive region and the materials loss itself reduces with the local decrease in carrier density, more light is now transmitted through the waveguide. This results in an increase in the output signal intensity (red curve in Figure 3a at 5 V). Based on the simulation, the modulation strength is 0.07 dB/ μm while the intrinsic loss due to material absorption is 0.51 dB/ μm. The simulated modulation qualitatively reproduces the experiments considering the ENZ effect.

A simulation without the benefits of the ENZ effect is also presented in Figure 3a (blue curve), where we assume that the real part of ITO permittivity ε_{real} remains unaffected and the imaginary part still changes with the applied bias. The resulting hypothetical material has the same material properties as in the experiment except the real part of permittivity in order to compare the situations with and without the ENZ effect. In this way, there is neither an ENZ effect nor an electrical field enhancement inside the ITO accumulation layer, while the material loss change is still considered. The variation in the material loss still leads to a modulation in the output signal intensity, but a much weaker modulation is observed than in the experiments.

The modulation strength can be further improved if the ENZ material is placed in the center of the waveguide, close to the field maximum in the mode profile. To this end, we created a 50 nm-wide slot in the waveguide and then introduced the HfO_2 gate oxide and the ITO material. In these experiments we used a waveguide width of 650 nm to maintain the same effective mode index as before. Figure 4a shows the optical mode profile supported by the waveguide with a single slot in the center and it shows an excellent mode overlap with the active ITO material, which conformally covers the waveguide. The new modulator goes through the same fabrication and post annealing process as the device shown in Figure 2 to allow for a fair performance comparison. Figure 4b shows a performance measurement of the modulator with the slot in the center (red curve), compared to the modulator without a slot (black curve). The signal modulation for a slot-waveguide modulator with a 30 μm length is 4.8 dB and the modulation strength is notably improved to 0.16 dB/μm. This result implies that a 3 dB modulator can be achieved with a 20 μm nonresonant waveguide-based device, while offering a broadband operation range (see Supporting Information). Due to the compact size, the modulator displays a small capacitance ($C \sim 0.4$ pF) as well and this results in a small dynamic energy per bit consumption ($\frac{1}{4}CV^2 \sim 2$pJ per bit).[32]

Whereas the goal of this work was to optimize and demonstrate the ENZ effect in a Si waveguide modulator, we also measured the modulation speed. Figure 4c shows that the highest modulation speed of the present devices was found to be 117 kHz, which is limited by the Si waveguide resistance (~MΩ) and the wiring capacitance,[17,18] while the inset demonstrates that the device response follows the gate bias with sharp edges robustly. The switching speeds for this modulator concept are ultimately limited by the fast movement of majority carriers and speeds up to many GHz should be feasible, as seen in other majority carrier-based devices.[6,7,33]

As the ENZ wavelength is determined by the carrier concentration of ITO, we are able to control the ENZ wavelength of ITO in the near-IR range by postannealing. As

DOI: 10.1021/acsphotonics.8b00945
ACS Photonics 2018, 5, 4484−4490

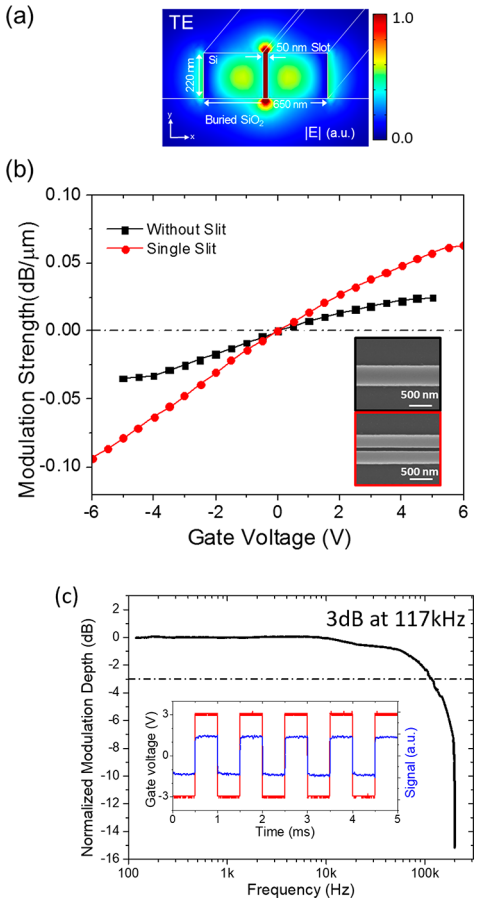

Figure 4. ENZ-based modulator with a single slot in the center and its modulation performance. (a) Electrical field distribution of the TE guided mode in the waveguide with a 50 nm-wide slot in the center without HfO_2 and ITO layer. The field is strongly concentrated inside the slot. (b) Measured modulation strength versus the applied gate voltage in the waveguide with a single slot (red curve) and without a slot (black curve). The insets show corresponding SEM images. (c) Modulator bandwidth measurement for our Si modulator with an ITO-filled slot. The normalized modulation depth versus the modulation frequency is plotted. The 3 dB switching speed is 117 kHz. The inserted figure shows the modulated signal intensity (blue line) under an AC bias of ±3 V (red line).

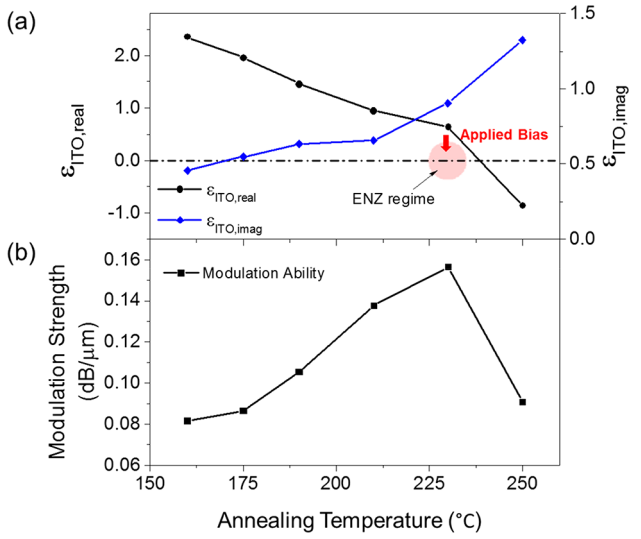

Figure 5. Material permittivity and modulation strength under various postannealing temperatures. (a) The permittivity of the ITO versus annealing temperature for 10 min forming gas anneals. The black line represents the real part and the blue line represents the imaginary part of the ITO film permittivity. The magnitude of the permittivity for the ITO annealed at 230 °C is closest to zero. By applying an electrical bias, an ENZ region is created along with strong electro-absorption results, as shown in the red highlighted area. (b) The modulation strength of ITO-based modulators with a single slot in the center and for various annealing temperatures in the range from 160 to 250 °C. The ITO annealed at 230 °C displays the largest modulation strength as it operates near the ENZ point.

the annealing temperature is raised from 160 to 250 °C, the electron density in the ITO film increases from 2.9×10^{20} cm^{-3} to 9.5×10^{20} cm^{-3}. The permittivity values from these films are obtained from ATR characterization (Figure 1b). Figure 5a shows the extracted permittivity of ITO at various annealing temperatures and Figure 5b shows the temperature dependence of the modulation strength in the unit of dB/μm. As the magnitude of the permittivity approaches zero, a stronger ENZ effect is observed and increases the modulation strength to 0.16 dB/μm at an annealing temperature of 230 °C. Once the permittivity crosses zero, the ITO turns metallic-like (i.e., exhibits a negative permittivity) and no ENZ enhancement in the modulation is achieved when an electrical bias is applied. This results in decrease in the modulation performance. Our analysis clearly shows the importance of tweaking the growth and annealing conditions of the ITO just right to achieve the highest possible performance.

To conclude, we have experimentally demonstrated an ENZ-based modulator employing a Si waveguide coated with an ITO/HfO_2 stack. We have demonstrated that it is critical to design the anneal treatment of the ITO to achieve a permittivity close to zero and realize the highest possible modulation depth. In this case, one can simultaneously benefit from enhanced local optical fields and an increased material loss due to the presence of more free carriers upon electrical gating. These points were verified with finite-element simulations. The work highlights that ENZ effects facilitate ultracompact, nonresonant modulator designs that can offer low energy consumption, high speed and broadband operation.

METHODS

Modulator Fabrication. The devices are fabricated using SOI wafers obtained from SIMGUI Co., with a nominal 220 nm device layer and 3.0 μm buried oxide layer. A JEOL JBX-6300FS electron-beam lithography system is used to pattern a ZEP-520A electron-beam resist layer spun on the samples, followed by a dry etching process to remove Si (Applied Materials Precision 5000 Etcher).[34] HfO_2 is conformally deposited on the device by atomic layer deposition (Savannah S200, Cambridge Nanotech). A second e-beam resist layer of PMMA is then spun on and patterned by the JEOL e-beam tool. The ITO layer was deposited by a DC magnetron sputtering process using an ITO ceramic target of In_2O_3 90 wt % /SnO_2 10 wt % with Ar and O_2 flow rates of 80 and 10 sccm, respectively. The sputtering power was 2 kW at 6.5 mTorr and the substrate temperature was kept below 80 °C. After deposition, a standard lift-off procedure is performed. The slot's width and waveguide dimensions are determined with SEM. The samples were diced into 1 cm × 1 cm size and postannealed under forming gas (5% H_2/95% N_2) to tune the carrier concentration of the ITO films at various temperatures between 160 to 250 °C for a duration of 10 min.[23]

DOI: 10.1021/acsphotonics.8b00945
ACS Photonics 2018, 5, 4484−4490

Electrical Measurements. For electric modulation experiments, the sample is provided with a 300 × 300 μm^2 Si contact pads and these are wire-bonded to a chip carrier. These pads are used to electrically contact the ITO layer and Si waveguide. A semiconductor parameter analyzer (Agilent Technologies B1500A) is used to apply a gate bias to the ITO/HfO_2/Si stack as well as performing IV measurements to quantify the breakdown voltage. Speed measurement are performed up to 200 kHz (see Supporting Information).

Optical Far-Field Detection. An uncollimated light source together with a thin glass slide is used to illuminate the sample for imaging purposes. The waveguide and grating couplers are imaged in reflection mode using an infrared InGaAs CCD camera (C10633-12, Hamamatsu Photonics K.K.). A collimated and linearly polarized near-infrared laser beam (New Focus 6300) is gently focused using a 10× objective lens onto the grating coupler to excite the optical mode in Si waveguide. The grating coupler is precisely aligned to the laser spot using a microposition stage. An iris diaphragm and a linear polarizer are used to only collect output light coming from output coupler. The signal intensity is measured by an ultrafast photodiode (Newport 818-BB-3) which allows us to perform accurate and fast speed intensity measurements. All of the waveguides are designed with a 90° bend so that the linearly polarized emission from the output of the waveguide is orthogonal to that of the input polarization, thus suppressing back-reflections coming from the incident beam and providing a good signal-to-noise ratio for the desired output signal.[4]

■ ASSOCIATED CONTENT

Supporting Information

The Supporting Information is available free of charge on the ACS Publications website at DOI: 10.1021/acsphotonics.8b00945.

(PDF)

■ AUTHOR INFORMATION

Corresponding Author

*E-mail: brongersma@stanford.edu.

ORCID

Kai Zang: 0000-0003-1488-3177

Mark L. Brongersma: 0000-0003-1777-8970

Funding

This work was supported by an AFOSR MURI program through Grant No. FA9550-17-1-0002 and an ONR MURI program through Grant No. N00014-12-1-0976.

Notes

The authors declare no competing financial interest.

■ REFERENCES

(1) Miller, D. A. B. Optical Interconnects to Silicon. *IEEE J. Sel. Top. Quantum Electron.* **2000**, *6* (6), 1312−1317.

(2) Miller, D. A. B. Device Requirements for Optical Interconnects to Silicon Chips. *Proc. IEEE* **2009**, *97* (7), 1166−1185.

(3) Kirchain, R.; Kimerling, L. A Roadmap for Nanophotonics. *Nat. Photonics* **2007**, *1* (6), 303−305.

(4) Lee, H. W.; Papadakis, G.; Burgos, S. P.; Chander, K.; Kriesch, A.; Pala, R.; Peschel, U.; Atwater, H. A. Nanoscale Conducting Oxide PlasMOStor. *Nano Lett.* **2014**, *14* (11), 6463−6468.

(5) Sorger, V. J.; Lanzillotti-Kimura, N. D.; Ma, R.-M. M.; Zhang, X. Ultra-Compact Silicon Nanophotonic Modulator with Broadband Response. *Nanophotonics* **2012**, *1* (1), 17−22.

(6) Liu, A.; Jones, R.; Liao, L.; Samara-Rubio, D.; Rubin, D.; Cohen, O.; Nicolaescu, R.; Paniccia, M. A High-Speed Silicon Optical Modulator Based on a Metal−oxide−semiconductor Capacitor. *Nature* **2004**, *427* (6975), 615−618.

(7) Xu, Q.; Schmidt, B.; Pradhan, S.; Lipson, M. Micrometre-Scale Silicon Electro-Optic Modulator. *Nature* **2005**, *435* (7040), 325−327.

(8) Miller, D. A. B.; Chemla, D. S.; Damen, T. C.; Gossard, A. C.; Wiegmann, W.; Wood, T. H.; Burrus, C. A. Band-Edge Electroabsorption in Quantum Well Structures: The Quantum-Confined Stark Effect. *Phys. Rev. Lett.* **1984**, *53* (22), 2173−2176.

(9) Liu, J.; Beals, M.; Pomerene, A.; Bernardis, S.; Sun, R.; Cheng, J.; Kimerling, L. C.; Michel, J. Waveguide-Integrated, Ultralow-Energy GeSi Electro-Absorption Modulators. *Nat. Photonics* **2008**, *2* (7), 433−437.

(10) Kuo, Y.-H.; Lee, Y. K.; Ge, Y.; Ren, S.; Roth, J. E.; Kamins, T. I.; Miller, D. a B.; Harris, J. S. Strong Quantum-Confined Stark Effect in Germanium Quantum-Well Structures on Silicon. *Nature* **2005**, *437* (7063), 1334−1336.

(11) Cai, W.; White, J. S.; Brongersma, M. L. Compact, High-Speed and Power-Efficient Electrooptic Plasmonic Modulators. *Nano Lett.* **2009**, *9* (12), 4403−4411.

(12) Liu, M.; Yin, X. B.; Ulin-Avila, E.; Geng, B. S.; Zentgraf, T.; Ju, L.; Wang, F.; Zhang, X. A Graphene-Based Broadband Optical Modulator. *Nature* **2011**, *474* (7349), 64−67.

(13) Ansell, D.; Radko, I. P.; Han, Z.; Rodriguez, F. J.; Bozhevolnyi, S. I.; Grigorenko, A. N. *Nat. Commun.* **2015**, *6*, 2−7.

(14) Vasudev, A. P.; Kang, J.-H.; Park, J.; Liu, X.; Brongersma, M. L. Electro-Optical Modulation of a Silicon Waveguide with An "epsilon-near-Zero" material. *Opt. Express* **2013**, *21* (22), 26387−26397.

(15) Liu, X.; Kang, J.-H.; Yuan, H.; Park, J.; Kim, S. J.; Cui, Y.; Hwang, H. Y.; Brongersma, M. L. Electrical Tuning of a Quantum Plasmonic Resonance. *Nat. Nanotechnol.* **2017**, *12*, 1−6.

(16) Feigenbaum, E.; Diest, K.; Atwater, H. A. Unity-Order Index Change in Transparent Conducting Oxides at Visible Frequencies. *Nano Lett.* **2010**, *10* (6), 2111−2116.

(17) Park, J.; Kang, J.-H.; Liu, X.; Brongersma, M. L. Electrically Tunable Epsilon-near-Zero (ENZ) Metafilm Absorbers. *Sci. Rep.* **2015**, *5*, 15754.

(18) Park, J.; Kang, J. H.; Kim, S. J.; Liu, X.; Brongersma, M. L. Dynamic Reflection Phase and Polarization Control in Metasurfaces. *Nano Lett.* **2017**, *17* (1), 407−413.

(19) Silveirinha, M. G.; Engheta, N. Theory of Supercoupling, Squeezing Wave Energy, and Field Confinement in Narrow Channels and Tight Bends Using ε near-Zero Metamaterials. *Phys. Rev. B: Condens. Matter Mater. Phys.* **2007**, *76* (24), 245109.

(20) Edwards, B.; Alù, A.; Young, M. E.; Silveirinha, M.; Engheta, N. Experimental Verification of Epsilon-near-Zero Metamaterial Coupling and Energy Squeezing Using a Microwave Waveguide. *Phys. Rev. Lett.* **2008**, *100* (3), 33903.

(21) Maas, R.; Parsons, J.; Engheta, N.; Polman, A. Experimental Realization of an Epsilon-near-Zero Metamaterial at Visible Wavelengths. *Nat. Photonics* **2013**, *7* (11), 907−912.

(22) Alù, A.; Silveirinha, M. G.; Salandrino, A.; Engheta, N. Epsilon-near-Zero Metamaterials and Electromagnetic Sources: Tailoring the Radiation Phase Pattern. *Phys. Rev. B: Condens. Matter Mater. Phys.* **2007**, *75* (15), 155410.

(23) Liu, X.; Park, J.; Kang, J. H.; Yuan, H.; Cui, Y.; Hwang, H. Y.; Brongersma, M. L. Quantification and Impact of Nonparabolicity of the Conduction Band of Indium Tin Oxide on Its Plasmonic Properties. *Appl. Phys. Lett.* **2014**, *105* (18), 181117.

(24) Franzen, S.; Rhodes, C.; Cerruti, M.; Gerber, R. W.; Losego, M.; Maria, J.-P.; Aspnes, D. E. Plasmonic Phenomena in Indium Tin Oxide and ITO-Au Hybrid Films. *Opt. Lett.* **2009**, *34* (18), 2867−2869.

(25) Abb, M.; Albella, P.; Aizpurua, J.; Muskens, O. L. All-Optical Control of a Single Plasmonic nanoantenna−ITO Hybrid. *Nano Lett.* **2011**, *11* (6), 2457−2463.

(26) Caspani, L.; Kaipurath, R. P. M.; Clerici, M.; Ferrera, M.; Roger, T.; Kim, J.; Kinsey, N.; Pietrzyk, M.; Di Falco, A.; Shalaev, V.

DOI: 10.1021/acsphotonics.8b00945
ACS Photonics 2018, 5, 4484−4490

M.; et al. Enhanced Nonlinear Refractive Index in Epsilon-near-Zero Materials. *Phys. Rev. Lett.* **2016**, *116* (23), 1−5.
(27) Losego, M. D.; Efremenko, A. Y.; Rhodes, C. L.; Cerruti, M. G.; Franzen, S.; Maria, J. P. Conductive Oxide Thin Films: Model Systems for Understanding and Controlling Surface Plasmon Resonance. *J. Appl. Phys.* **2009**, *106* (2), 24903.
(28) Van Laere, F.; Claes, T.; Schrauwen, J.; Scheerlinck, S.; Bogaerts, W.; Taillaert, D.; O'Faolain, L.; Van Thourhout, D.; Baets, R. Compact Focusing Grating Couplers for Silicon-on-Insulator Integrated Circuits. *IEEE Photonics Technol. Lett.* **2007**, *19* (21−24), 1919−1921.
(29) Taillaert, D.; Van Laere, F.; Ayre, M.; Bogaerts, W.; Van Thourhout, D.; Bienstman, P.; Baets, R. Grating Couplers for Coupling between Optical Fibers and Nanophotonic Waveguides. *Jpn. J. Appl. Phys.* **2006**, *45* (8A), 6071−6077.
(30) Vlasov, Y. A.; McNab, S. J. Losses in Single-Mode Silicon-on-Insulator Strip Waveguides and Bends. *Opt. Express* **2004**, *12* (8), 1622−1631.
(31) King, P. D. C.; Veal, T. D.; McConville, C. F. Nonparabolic Coupled Poisson-Schrödinger Solutions for Quantized Electron Accumulation Layers: Band Bending, Charge Profile, and Subbands at InN Surfaces. *Phys. Rev. B: Condens. Matter Mater. Phys.* **2008**, *77* (12), 1−7.
(32) Miller, D. a. B. Energy Consumption in Optical Modulators for Interconnects. *Opt. Express* **2012**, *20* (S2), A293.
(33) Chen, G.; Chen, H.; Haurylau, M.; Nelson, N. A.; Albonesi, D. H.; Fauchet, P. M.; Friedman, E. G. Predictions of CMOS Compatible on-Chip Optical Interconnect. *Integr. VLSI J.* **2007**, *40* (4), 434−446.
(34) Piggott, A. Y.; Lu, J.; Lagoudakis, K. G.; Petykiewicz, J.; Babinec, T. M.; Vučković, J. Inverse Design and Demonstration of a Compact and Broadband on-Chip Wavelength Demultiplexer. *Nat. Photonics* **2015**, *9* (May), 374−377.

DOI: 10.1021/acsphotonics.8b00945
ACS Photonics 2018, 5, 4484−4490